

Detection of Thermal Emission of XO-2b: Evidence for a Weak Temperature Inversion

Pavel Machalek^{1,2}, Peter R. McCullough², Adam Burrows³, Christopher J. Burke⁴,
Joseph L. Hora⁴, Christopher M. Johns-Krull⁵

pavel@jhu.edu

ABSTRACT

We estimate flux ratios of the extrasolar planet XO-2b to its host star XO-2 at 3.6, 4.5, 5.8 and 8.0 micron with IRAC on the *Spitzer Space Telescope* to be 0.00081 ± 0.00017 , 0.00098 ± 0.00020 , 0.00167 ± 0.00036 and 0.00133 ± 0.00049 , respectively. The fluxes provide tentative evidence for a weak temperature inversion in the upper atmosphere, the precise nature of which would need to be confirmed by longer wavelength observations. XO-2b substellar flux of 0.76×10^9 ergs cm⁻² s⁻¹ lies in the predicted transition region between atmospheres with and without upper atmospheric temperature inversion.

Subject headings: stars:individual(XO-2) — binaries:eclipsing — infrared:stars — planetary systems

1. Introduction

The field of comparative planetology has burgeoned in the past year (Deming 2009): four exo-planet secondary eclipse observations have been published with all four IRAC

¹Department of Physics and Astronomy, Johns Hopkins University, 3400 North Charles St., Baltimore MD 21218

²Space Telescope Science Institute, 3700 San Martin Dr., Baltimore MD 21218

³Department of Astrophysical Sciences, Princeton University, Princeton, NJ 08544

⁴Harvard-Smithsonian Center for Astrophysics, 60 Garden St., Cambridge, MA 02138

⁵Department of Physics and Astronomy, Rice University, 6100 Main Street, MS-108, Houston, TX 77005

channels: HD 209458b (Knutson et al. 2008); HD 189733b (Charbonneau et al. 2008); XO-1b (Machalek et al. 2008) and TrES-4 (Knutson et al. 2009), which were used to deduce the temperatures structure in the planetary upper atmospheres. Numerous scientific firsts were also announced: a model dependent derivation of the radiative time constant of an extrasolar planet atmosphere (Laughlin et al. 2009), first unambiguous detection of water vapor in a Hot Jupiter atmosphere in HD 189733b (Grillmair et al. 2008), together with prospects for detailed study of extrasolar planet atmospheres with JWST (Seager et al. 2008).

Planetary stratospheres, which are common in the giant planets of the Solar System (de Pater & Lissauer 2001), form when high stellar flux penetrates deep into the atmosphere where the atmosphere does not efficiently radiate the heat away. Hot-Jupiters were also observed to possess stratospheres (Knutson et al. 2008; Machalek et al. 2008; Knutson et al. 2009) and enhanced opacity at high altitude in the form of an extra absorber of optical light has been suggested as the physical cause of upper atmospheric temperature inversions (Hubeny et al. (2003); Burrows et al. (2008); Fortney et al. (2008)). Spiegel et al. (2009) have recently argued against vanadium oxide (VO) as the extra optical absorber and suggested that even the previously favored gaseous optical absorber titanium oxide (TiO) would probably rain out of the upper atmosphere unless unusually high levels of macroscopic mixing exist (Eddy diffusion coefficients $K_{zz} \sim 10^7\text{-}10^{11}$ depending on particulate size of the TiO condensates) compared to Jupiter ($K_{zz} \sim 10^6$ (de Pater & Lissauer 2001)) to overcome gravitational settling. Zahnle et al. (2009) has considered the role by which absorption of UV and visible light by S_2 and S_3 can lead to formation of thermal inversion in upper atmospheres of Hot-Jupiters and suggested planetary metallicity, in addition to substellar flux, as the determining factor for the presence of a temperature inversion.

Hot-Jupiter atmosphere models (Burrows et al. 2007a, 2008; Spiegel et al. 2009; Fortney et al. 2008) show that water and CO opacity define the $\tau=2/3$ decoupling layers and the relative temperatures at those layers determine the relative brightness at 3.6 micron and 4.5 micron. In the presence of an optical absorber in the upper atmosphere the 4.5 micron planet flux is higher than the 3.6 micron flux and vice-versa for models without an optical absorber in the upper atmosphere, which serves as an important diagnostic for detection of thermal inversions in upper atmospheres of Hot-Jupiters (see Fig. 1 for the XO-2b Temperature / Pressure profile).

A detailed study of the IR secondary eclipse planetary spectra of HD 209458b, HD 189733b, TrES-1, HD 149026b and non-eclipsing HD 179949b, and v And b by Burrows et al. (2008) suggests that the presence of such an upper atmospheric absorber might be dependent

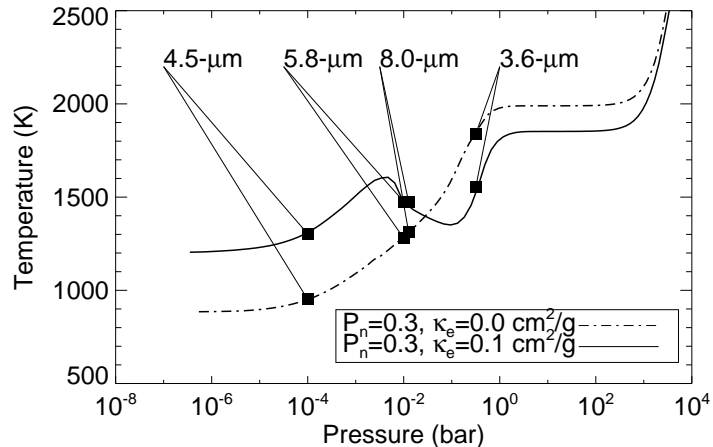


Fig. 1.— (top) Temperature / Pressure profiles for the atmosphere of XO-2b following the methodology of Burrows et al. (2007a, 2008); Spiegel et al. (2009) for heat redistribution parameter $P_n=0.3$ with no upper atmospheric optical absorber (dot-dashed line) and a corresponding model with a uniform upper atmospheric absorber (solid line) (absorption coefficient $\kappa_e=0.1 \text{ cm}^2/\text{g}$) with depths corresponding to emission in the IRAC channels denoted.

on the flux from the star at the sub-stellar point on the planet as well as second order effects like metallicity and planetary surface gravity. In the Burrows et al. (2008) interpretation planets with high sub-stellar point flux (e.g., HD 209458b, OGLE-Tr-56b, OGLE-Tr-132b, TrES-2b and XO-3b) would have extra optical absorber in the upper atmospheric layer and water features in emission while planets with lower fluxes (XO-1b, TrES-1, XO-2b and HD 189733b) would have no such extra absorber and would possess water features in absorption. Fortney et al. (2008) also suggest a similar division of planetary spectra based on incident stellar flux. Observations of XO-2b and other planetary systems directly constrain and test the incident flux threshold necessary for the occurrence for a thermal inversion in the upper atmosphere of a Hot-Jupiter.

Based on the planetary sub-stellar point flux from the star, both Burrows et al. (2008) and Fortney et al. (2008) predicted that XO-1b should not have exhibited a thermal inversion in its upper atmosphere, yet a temperature inversion is observed (Machalek et al. 2008). The incident flux on XO-2b from its parent star ($0.76 \times 10^9 \text{ ergs cm}^{-2} \text{ s}^{-1}$) lies in the predicted transition region between upper atmospheres with or without thermal inversions as delineated by Burrows et al. (2008); Fortney et al. (2008). Burrows et al. (2008) predicted a “weak stratosphere” for XO-2b.

XO-2 (2MASS J07480647+5013328) has high metallicity, $[\text{Fe}/\text{H}]=0.45 \pm 0.02$, high proper motion, $\mu_{\text{tot}}=157 \text{ mas yr}^{-1}$, and a common proper motion stellar companion with $31''$ separation (Burke et al. 2007). The planet XO-2b has an orbital period of 2.6158640 ± 0.0000016 days (Fernandez et al. 2009) and orbits around the northern declination component of the XO-2 stellar binary system (see Fig. 2) . We present observations of the infrared spectral energy distribution (SED) of the planet XO-2b (Burke et al. 2007) in all 4 IRAC channels obtained during secondary eclipses observed with *Spitzer Space Telescope*. By comparing XO-2b’s SED with atmospheric models, we test for the presence of a thermal inversion in the upper atmosphere of XO-2b.

2. Observations

The InfraRed Array Camera (IRAC; Fazio et al. 2004) has a field of view of $5.2' \times 5.2'$ in each of its four bands. Two adjacent fields are imaged in pairs (3.6 and 5.8 microns; 4.5 and 8.0 microns). The detector arrays each measure 256×256 pixels, with a pixel size of approximately $1.22'' \times 1.22''$. We have observed the XO-2b system in all 4 channels in two separate Astronomical Observing Requests (AORs) in two different sessions: the 3.6 and 5.8 micron channels for 5.94 hours on UT 2007 November 16 (AOR 24462080) and the 4.5 and 8.0 micron channels for 5.94 hours on UT 2007 November 19 (AOR 24462336). We used the full array 2s+2s/12s frame time in the stellar mode in which the 3.6 micron and 4.5 micron bands are exposed for two consecutive 2s exposures while the 5.8 micron and 8.0 micron bands are integrating for 12s to prevent detector saturation. Figure 2 shows a representative IRAC 3.6 micron image.

We used the standard IRAC Basic Calibrated Data (BCD) products (version 16.1) described in the Spitzer Data Handbook¹, which includes dark frame subtraction, multiplexer bleed correction, detector linearization, and flat-fielding of the images. The starting point for our analysis were the BCD images. We converted the times recorded by the spacecraft in the FITS file header keyword DATE-OBS to heliocentric Julian dates using the orbital ephemeris of the spacecraft provided by the Horizons Ephemeris System². We flagged cosmic ray pixels in the images, which resulted in [0.8; 0.4; 2.4; 3.1] % of photometric points in the [3.6; 4.5; 5.8 and 8.0] micron time series to have a flagged pixel in the photometric aperture and which were not used in the analysis. We did not resample the pixels in any way during our analysis doing so could compromise the photometry.

¹<http://ssc.spitzer.caltech.edu/irac/dh/>

²<http://ssd.jpl.nasa.gov/>

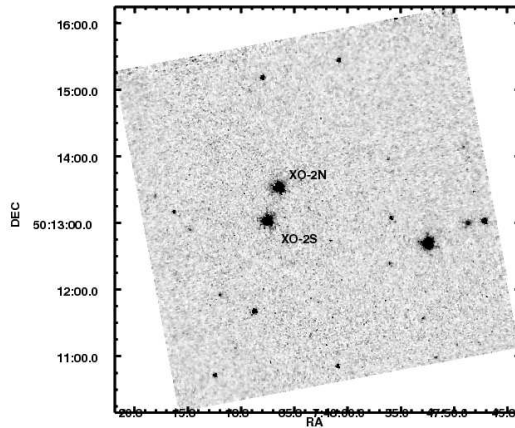


Fig. 2.— The field-of-view of the XO-2 binary system in the IRAC 3.6 micron channel. North is up, East is to the left. XO-2N hosts the transiting extrasolar planet XO-2b.

To determine the scalar background for the photometry we subtracted the zodiacal background in each channel by constructing a histogram of all pixels in each image and fitting a Gaussian to the distribution of the zodiacal background brightness. We evaluated the centroids of both North and South components of XO-2b with the IDL CNTRD routine which locates where the second derivatives of x and y pixel position reach 0. We have found that CNTRD centroids have lower rms in both x and y pixel directions than the centroids produced by IDL routine GCNTRD, which fits Gaussians to marginal x and y distributions. The pointing in the 3.6 micron channel varied by ~ 0.10 pixels in x and ~ 0.06 pixels peak-to-peak in y and by ~ 0.15 pixel in x and ~ 0.20 pixel in y in the 4.5 micron channel. The shifting of the stellar centroid within a pixel, which have sub-pixel sensitivity variations, resulted in a modulation of the stellar flux in the 3.6 micron and 4.5 micron channels (described below).

2.1. 3.6 and 4.5 micron time series

We performed aperture photometry on the 3.6 micron and 4.5 micron background subtracted images with aperture radii ranging from 2.5 to 5.0 pixels in 0.5 pixel increments for both components of the XO-2 binary. The sky level was elevated during the first hour of observations in the 3.6 micron channel (see Fig. 3). This behavior is opposite the asymptotic behavior in the 3.6 micron channel for the similarly bright star TrES-4 (Knutson et al. 2009). The 3.6 micron and 4.5 micron time series exhibited a sharp increase during the

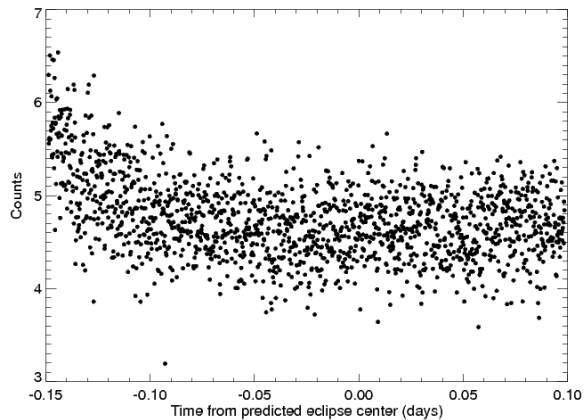


Fig. 3.— The average sky count rates in the annulus with radii between 13 and 50 pixels around the star XO-2N for the 3.6 micron IRAC channel observations. Notice the asymptotic increase of the sky count rates in the first ~ 1 hour of observation. Similar trend was observed for the other binary component XO-2S.

first ~ 20 minutes of exposure for XO-2 and the 2 calibrators, presumably as a result of the instrument reaching a new equilibrium after previous observations. Such relaxation effects can reach several percent and usually stabilize within the first hour of observations of a new target. We have rejected the first 180 points in the 3.6 micron and 4.5 micron time series.

The aperture radius was selected by choosing the lowest rms for out-of-eclipse points. Aperture of 2.5 pixels was chosen for the 3.6 micron time series, with an out-of-eclipse rms of 0.0044 after systematic effect removal which is 1.02 times the photon noise limit based on stellar brightness, background flux and detector read noise. Similarly, for the 4.5 micron series an aperture of 2.5 pixels resulted in the lowest out-of-eclipse rms of 0.0063 which is 1.05 times the photon noise limit. We applied the appropriate aperture correction for each channel to the stellar flux value according to the Spitzer Data Handbook of [1.112, 1.113, 1.125, 1.218] for the [3.6, 4.5, 5.8 and 8.0] micron channels, respectively.

A strong correlation between the sub-pixel centroid and stellar brightness was observed in both the 3.6 micron and 4.5 micron channels, with flux amplitudes of $\sim 1.3\%$ and 0.5% , respectively. This well studied effect (Charbonneau et al. 2005; Morales-Calderón et al. 2006; Machalek et al. 2008; Knutson et al. 2009) is due to the InSb detector intrapixel sensitivity variations as the spacecraft jitters $\sim 0.1 - 0.3$ arcsec in orientation over a period of ~ 3000 seconds³. The uncorrected sub-pixel intensity variations are clearly visible in the time

³<http://ssc.spitzer.caltech.edu/documents/exoplanetmemo.txt>

series of XO-2 in the 3.6 micron and 4.5 micron channels in Fig. 4.

Despite the similarity between the XO-2 stellar binary components (same brightness $J = 9.74 \pm 0.02$ and similar color $(J-H)_{NORTH} = 0.40 \pm 0.03$ vs. $(J-H)_{SOUTH} = 0.37 \pm 0.03$) the amplitude of their the sub-pixel sensitivity variations in the 3.6 micron channel for the North and South component of XO-2b is markedly different (1.3 % for XO-2N vs 0.7% for XO-2S, see Fig. 4). This is most likely due to the different positions of the two XO-2 components with respect to the edge of the pixel and hence being affected differently by the pixel response function. Laughlin et al. (2009) have noted in their 30-hour long 8.0 micron time series of the HD80606 and HD80607 binary components, which also have same brightness and similar color, that due to different sub-pixel positions the detector systematic ramps are different.

We have corrected for the sub-pixel intensity variations by fitting a function of 4 variables to the time series of XO-2b :

$$I_{subpixel} = b_1 + b_2x + b_3y + b_4t, \quad (1)$$

where b_i are coefficients; x and y are subpixel centroids of the stellar flux and t is the time from the start of observations in days. We have tried quadratic and cross terms for the subpixel centroids correction (Desert et al. 2009) but that has not improved our χ^2 and hence were not used. We fit the secondary eclipse light curves using the formalism of Mandel & Agol (2002) with no stellar limb darkening as appropriate for a secondary eclipse. We adopt stellar and planetary parameters from Burke et al. (2007) ⁴ : $R_\star = 0.97^{+0.02}_{-0.02} R_\odot$, $R_p = 0.98^{+0.03}_{-0.03} R_{Jup}$ ⁵, $i = 88.9^{+0.7}_{-0.7}$ degrees, and $a = 0.0369 \pm 0.0002$ AU with updated ephemeris from Fernandez et al. (2009):

$$T_c(E) = 2,454,466.884670(HJD) + E(2.6158640 \text{ days}). \quad (2)$$

We have fitted the 4 baseline detrending parameters (a constant, linear x-position, linear y-position and linear time terms) concurrently with the depth of the eclipse ΔF and the timing of the centroid ΔT (total of 6 fitting parameters) using a Monte Carlo Markov Chain (MCMC) with 10^5 iterations such that the ratio of jumps for each parameter was between 20-40 % (see Gregory (2005); Markwardt (2009)). The initial 20% iterations were rejected

⁴We have redone the entire analysis using the updated planetary and stellar parameters of Fernandez et al. (2009) and our results do not change withing uncertainties.

⁵ $1 R_{Jup} = 71,492$ km.

to remove arbitrary starting conditions and the final parameters were chosen as the median value from the posterior probability distribution for each parameter. The adopted eclipse depth ΔF and centroid timing ΔT in minutes from the expected secondary eclipse mid-center time for an assumed eccentricity of zero are reported in Table 1 with errors obtained from the symmetric 66.8 % contours around the median of the posterior probability distribution from the MCMC runs. Best-fit eclipse curves binned in 6.0-minute intervals are plotted in Fig. 5 and the eclipse parameters are listed in Table 1. They are the channel wavelength, eclipse depth ΔF , eclipse mid-center time in HJD and the timing offset ΔT .

We find that the 3.6 micron time series of XO-2b exhibits a linear flux trend with a slope of $b_4 = -0.011\% \pm 0.005\%$ per hour. This trend is consistently removed from our time series by including a linear time term b_4 as one of the MCMC 6 parameter fit, as described above. Knutson et al. (2009) noted a linear trend in their 3.6 micron time series of TrES-4 with a slope of $+0.030 \pm 0.004\%$ per hour and attributed such linear trend to a previously unknown instrumental effect of the detector. The 4.5 micron time series of XO-2b exhibits a similar linear trend to the 3.6 micron time series with a slope of $-0.010\% \pm 0.004\%$ per hour, which is lower than a corresponding slope for TrES-4 of $-0.020 \pm 0.003\%$ per hour (Knutson et al. 2009) even though XO-2N is 11 times brighter.

To assess the amount of non-Gaussian correlated red noise left in the time series after systematic effect removal we have performed the complete MCMC analysis on the other binary component XO-2S in the XO-2 binary system, which does not have a short-period Jovian mass orbiting it (which would have easily been detected by radial velocity observations) and thus does not exhibit a secondary eclipse. The best fit eclipse curves of XO-2S are plotted on the right in Fig. 5. The 3.6 micron, 5.8 micron and 8.0 micron channels exhibit eclipse depths consistent with zero while the 4.5 micron channel shows an eclipse with depth 0.00064 ± 0.00033 based on Gaussian statistics with a time shift of $+11.1 \pm 24.8$ min. We exclude the possibility that the spurious eclipse at 4.5 micron around XO-2S could be due to a transiting super-Earth (corresponding to $R_p = 2.4R_\oplus$ around XO-2S) by noting that the eclipse is not observed in the 8.0 micron time series of XO-2S, which allows for maximum depths of 0.00002 ± 0.00001 and since it was observed at the same time as the 4.5 micron time series we can reject the transiting super-Earth hypothesis at more than $10\text{-}\sigma$.

The significant non-zero eclipse depth around the control star XO-2S which does not have short-period Jovian-mass planet suggests that the 4.5 micron time series for both XO-2N and XO-2S underestimates the amount of time correlated red-noise even after our calibration procedures.

2.2. 5.8 and 8.0 micron time series

Aperture photometry was performed on the images with cosmic ray pixels flagged with an aperture radius between 2.5 and 6.0 pixels in 0.5 pixel increments. The optimal size of the aperture was determined by minimizing the rms scatter in the light curve for observations outside of the eclipse. Aperture of 3.5 pixels was chosen for the 5.8 micron time series, with an out-of-eclipse rms of 0.0066 which is 32 % greater than the theoretical noise based on stellar brightness, background flux and detector read noise. Similarly for the 8.0 micron series an aperture of 4.0 pixels resulted in the lowest out-of-eclipse rms of 0.0054 which is 35% higher than the photon noise limit. The internal scattering of photons inside 5.8 micron and 8.0 micron Si:As arrays is likely responsible for the fact that we do not approach the Poisson limit as closely as in the 3.6 micron and 4.5 micron channels.⁶ Unlike for the XO-1b observations Machalek et al. (2008), where the first ~ 30 minutes of observations were rejected as the instrument settled into a new equilibrium state, we do not observe such an initial ramp-up in the 5.8 micron and 8.0 micron time series and conversely we do not reject any data points from the beginning of the time series in these channels.

Fig. 4 shows intensity variation with time, which is caused by changes in the effective gain of individual pixels over time. This effect has been observed before by Deming et al. (2005), both in the IRAC camera and in the IRS and MIPS 24 micron cameras and is dependent on the illumination level of the individual pixel (Knutson et al. 2007, 2008). Pixels with high illumination will reach their equilibrium within ~ 1 hour, but lower illumination pixels increase in intensity over time, approximately proportional to the inverse of the logarithm of illumination. The detector ramp intensity in the 5.8 micron time series decreased in flux during the ~ 6 hours of observation by ~ 0.1 % for XO-2N and by ~ 0.5 % for XO-2S, following a similar trend seen by Knutson et al. (2008) in their 5.8 micron time series of brighter HD 209458b.

We detect a nonlinear increase in the brightness of XO-2N and XO-2S in the 8.0 micron channel similarly to Knutson et al. (2007) who have reported a nonlinear flux increase over time with the 8.0 micron IRAC detector. Most recently the gain variation with time and illumination has been confirmed in the extended duration (30 hours) observations of HD80606 and HD80607 (Laughlin et al. 2009), who found that even for similarly bright and similar color binary, the 5.8 micron and 8.0 micron time series “ramp” can be different, presumably due to different position of the stars in relation to the edge of the pixels.

To properly account for the way in which the non-linear flux ramps affect our estimate

⁶http://ssc.spitzer.caltech.edu/documents/irac_memo.txt

of the secondary eclipse depth and timing we have performed MCMC simultaneous fitting of the 3 ramp parameters (see Eq. 3) and the eclipse depth ΔF and centroid timing ΔT (5 parameter fit overall):

$$I_{model} = a_1 + a_2 \times \ln(\Delta t + 0.05) + a_3 \times (\ln(\Delta t + 0.05))^2, \quad (3)$$

where I_{model} is the normalized model flux, Δt is the time in days since the beginning of observations (the 0.05 factor is included to prevent singularity at $\Delta t = 0$) and a_i are coefficients.

The MCMC fitting was performed in the same way as for the 3.6 micron and 4.5 micron channels with uncertainties obtained from the symmetric 66.8 % contours around the median of the posterior probability distribution from the MCMC runs. The eclipse depth in the 5.8 micron channel of 0.00167 ± 0.00036 represents an overall $4.7\text{-}\sigma$ detection of the secondary eclipse based on the cumulative SNR of all the in-eclipse points and similarly the 8.0 micron channel eclipse of 0.00133 ± 0.00049 has an overall SNR of 2.7. The resultant time series were normalized using out-of-eclipse points and binned into 6.0-minute bins (Fig. 5) for viewing clarity.

3. Discussion

To check whether our results depend on the aperture radius we have redone the MCMC analysis for photometry with aperture radii between 2.5 and 4.5 pixels for the 3.6 micron and 4.5 micron time series and aperture radii from 3.0 to 5.0 pixels in the 5.8 micron and 8.0 micron time series and obtained consistent results for the eclipse depth ΔF and centroid timing ΔT within errors to our adopted values from Table 1.

To test the robustness of our data reduction and MCMC analysis technique and consistency with other observations in the IRAC full-array mode we have reanalyzed the IRAC secondary eclipse time series of XO-1 from Machalek et al. (2008) in all 4 IRAC channels with the new MCMC pipeline. The eclipse depths ΔF of XO-1b with our MCMC pipeline are still in agreement with a model of a thermal inversion and an extra upper atmospheric absorber of uniform opacity of $\kappa_e = 0.1 \text{ cm}^2/\text{g}$ and redistribution parameters of $P_n = [0.3]$ at $[1.8, 0.8, 0.4]\text{-}\sigma$ at 3.6 micron, 4.5 micron and 5.8 micron bands, respectively. The secondary eclipse of XO-1b in the current MCMC analysis of 8.0 micron time series is $3.8\text{-}\sigma$ above the thermal inversion model above but clearly inconsistent at $16.1\text{-}\sigma$ with an atmospheric model without a temperature inversion. Our conclusion from Machalek et al. (2008) for a temperature inversion in the upper atmosphere of XO-1b caused by an optical absorber of uniform opacity of $\kappa_e = 0.1 \text{ cm}^2/\text{g}$ is thus reinforced. We have thus demonstrated that our

MCMC reduction and analysis pipeline is robust and the secondary eclipse depth estimates are consistent with previous pipeline versions from Machalek et al. (2008).

The eclipse mid-center timings for XO-2b in Table 1 are individually consistent within uncertainties with zero timing residuals for a circular orbit based on the ephemeris by Fernandez et al. (2009) and a combined mid-eclipse timing offset of -1.0 ± 9.7 min. Using the equation of (e.g. Kopal (1959) Eq. 9.23):

$$e \times \cos(\omega) \simeq \frac{\pi \Delta t}{2P}, \quad (4)$$

where e is the eccentricity, ω is the longitude of periastron, P is the orbital period, and Δt is the centroid time shift from expected time of secondary eclipse, allows us to set a 3- σ upper limit on $e \times \cos(\omega) < 0.012$.

The XO-2b eclipse depths in Fig. 6 show several trends. The flux ratio of XO-2b to the star peaks in the 5.8 micron channel, with a decrease towards the 3.6 micron and 4.5 micron channels and a slight decrease towards the 8.0 micron channel. The solid line and band averages represented as open squares in Fig. 6 depict an atmospheric model of XO-2b, following the methodology of Burrows et al. (2007a, 2008); Spiegel et al. (2009) with a thermal inversion and an extra upper atmospheric absorber of uniform opacity of $\kappa_e = 0.1 \text{ cm}^2/\text{g}$ and redistribution parameters of $P_n = [0.3]$. $P_n=0$ corresponds to no heat redistribution from the planetary day-side to the night-side and $P_n = 0.5$ stands for full redistribution (see Burrows et al. (2008) for details). The upper atmospheric temperature inversion model fits the observed eclipse depths within 1.0- σ in the 3.6 micron, 4.5 micron and 5.8 micron bands, respectively, while the 8.0 micron channel eclipse depth is offset by -1.4- σ from the model. The model without an upper atmospheric temperature inversion with the redistribution parameter $P_n = [0.3]$ (dot-dashed curves) does not fit the observations by [1.6, 2.2]- σ , respectively, in the 4.5 micron and 5.8 micron channels while fitting the 3.6 micron and 8.0 micron band eclipse depth within 1.0- σ . The eclipse depth fit in the 3.6 micron, 4.5 micron and 5.8 micron bands thus provides evidence for a “weak” temperature inversion in the upper atmosphere of XO-2b. XO-2b would thus be the second Hot-Jupiter along with XO-1b with a sub-stellar point flux of less than $\sim 1.0 \times 10^9 \text{ erg cm}^{-2} \text{ s}^{-1}$ to possess a temperature inversion in its upper atmosphere.

The possibility of thermal inversion in a planetary upper atmosphere has been suggested by Hubeny et al. (2003); Iro et al. (2005); Burrows et al. (2006, 2007a) and Fortney et al. (2008). A thermal inversion in the planetary upper atmosphere has been invoked for interpretation of broadband IR spectra in the case of HD209458b (Knutson et al. 2008);

XO-1b (Machalek et al. 2008); HD149026b (Harrington et al. 2007) and recently TrES-4 (Knutson et al. 2009). The presence of an extra optical absorber in the upper atmosphere, of yet unknown composition, would yield a thermal inversion in the planetary upper atmosphere and the presence of the water features in emission.

Burrows et al. (2008) and Fortney et al. (2008) suggested that the presence of the extra optical absorber in the upper atmosphere might be correlated with the incident flux from the star at the sub-stellar point on the planet. XO-2b substellar flux of (0.76×10^9 ergs $\text{cm}^{-2} \text{s}^{-1}$) lies in the transition region between atmospheres with or without upper atmospheric temperature inversions. XO-1b which has an even lower substellar flux of 0.49×10^9 ergs $\text{cm}^{-2} \text{s}^{-1}$ yet possesses unambiguous signs of a temperature inversion in the upper atmosphere, which suggests that secondary effects like metallicity (Zahnle et al. 2009) and planetary surface gravity may also determine the nature of the temperature inversion of the upper atmospheres of Hot-Jupiters.

Confirmation of the weak temperature inversion of XO-2b would be possible with longer wavelength observations because the contrast between models with or without a thermal inversion is high (see Fig. 6). Further study of Hot-Jupiter upper atmospheres, especially of planets that lie in the predicted transition region of the substellar flux ($\sim 0.6 - 1.0 \times 10^9$ ergs $\text{cm}^{-2} \text{s}^{-1}$) like HAT-P-1, WASP-2b, HD197286, should refine the sub-stellar flux boundary with respect to the presence/absence of an upper atmospheric thermal inversion.

4. Conclusion

We report the estimated flux ratios of the planet XO-2b in the *Spitzer Space Telescope* IRAC 3.6, 4.5, 5.8 and 8.0 micron channels. The fluxes are consistent with a weak temperature inversion in the upper atmosphere of XO-2b. The atmospheric model with an upper atmospheric temperature inversion with an extra optical absorber of opacity of $\kappa_e = 0.1 \text{ cm}^2/\text{g}$ and redistribution parameter $P_n=0.3$ provides the best fit to the data in the 3.6 micron, 4.5 micron and 5.8 micron channels with a mild $-1.4\text{-}\sigma$ inconsistency in the 8.0 micron channel.

The presence or absence of the stratospheric absorber and thermal inversion layer has been linked to the flux from the parent star at the sub-stellar point on the planet. The XO-2b sub-stellar point flux of $\sim 0.76 \times 10^9$ erg $\text{cm}^{-2} \text{s}^{-1}$ is the second lowest so far reported for a planetary atmosphere with a thermal inversion.

The authors would like to thank H. Knutson and N. Iro for helpful discussions. The authors would also like to acknowledge the use of publicly available routines by Eric Agol and Levenberg-Marquardt least-squares minimization routine MPFITFUN by Craig Markwardt. P.M. and P.R.M. were supported by the Spitzer Science Center Grant C4030 to the Space Telescope Science Institute. A.B. was supported in part by NASA grant NNX07AG80G. We also acknowledge support through JPL/Spitzer Agreements 1328092, 1348668, and 1312647. This work is based on observations made with the Spitzer Space Telescope, which is operated by the Jet Propulsion Laboratory, California Institute of Technology under a contract with NASA. This publication also makes use of data products from the Two Micron All Sky Survey, which is a joint project of the University of Massachusetts and the Infrared Processing and Analysis Center/California Institute of Technology, funded by the National Aeronautics and Space Administration and the National Science Foundation.

REFERENCES

- Burke, C. J., et al. 2007, *ApJ*, 671, 2115
- Burrows, A., Sudarsky, D., & Hubeny, I. 2006, *ApJ*, 650, 1140
- Burrows, A., Hubeny, I., Budaj, J., Knutson, H. A., & Charbonneau, D. 2007a, *ApJ*, 668, L171
- Burrows, A., Budaj, J., & Hubeny, I. 2008, *ApJ*, 678, 1436
- Charbonneau, D., et al. 2005, *ApJ*, 626, 523
- Charbonneau, D., Knutson, H. A., Barman, T., Allen, L. E., Mayor, M., Megeath, S. T., Queloz, D., & Udry, S. 2008, *ApJ*, 686, 1341
- Deming, D., Seager, S., Richardson, L. J., & Harrington, J. 2005, *Nature*, 434, 740
- Deming, D. 2009, *IAU Symposium*, 253, 197
- de Pater, I., & Lissauer, J. J. 2001, *Planetary Sciences*, by Imke de Pater and Jack J. Lissauer, pp. 544. ISBN 0521482194. Cambridge, UK: Cambridge University Press, December 2001., p.69
- Desert, J.-M. et al. 2009, arXiv:0903.3405
- Fazio, G. G. et al. 2004, *ApJS*, 154, 10
- Fernandez, J. M., Holman, M. J., Winn, J. N., Torres, G., Shporer, A., Mazeh, T., Esquerdo, G. A., & Everett, M. E. 2009, *AJ*, 137, 4911
- Fortney, J. J., Lodders, K., Marley, M. S., & Freedman, R. S. 2008, *ApJ*, 678, 1419
- Gregory, P. C. 2005, *Bayesian Logical Data Analysis for the Physical Sciences: A Comparative Approach with ‘Mathematica’ Support*. Edited by P. C. Gregory. ISBN 0 521 84150 X (hardback); Cambridge University Press, Cambridge, UK, 2005

Grillmair, C. J., et al. 2008, *Nature*, 456, 767
Harrington, J., Luszcz, S., Seager, S., Deming, D., & Richardson, L. J. 2007, *Nature*, 447, 691
Hubeny, I., Burrows, A., & Sudarsky, D. 2003, *ApJ*, 594, 1011
Iro, N., Bézard, B., & Guillot, T. 2005, *A&A*, 436, 719
Knutson, H. A., et al. 2007a, *Nature*, 447, 183
Knutson, H. A., Charbonneau, D., Allen, L. E., Burrows, A., & Megeath, S. T. 2008, *ApJ*, 673, 526
Knutson, H. A., Charbonneau, D., Burrows, A., O’Donovan, F. T., & Mandushev, G. 2009, *ApJ*, 691, 866
Kopal, Z. 1959, *The International Astrophysics Series*, London: Chapman & Hall, 1959,
Laughlin, G., Deming, D., Langton, J., Kasen, D., Vogt, S., Butler, P., Rivera, E., & Meschiari, S. 2009, *Nature*, 457, 562
Machalek, P., McCullough, P. R., Burke, C. J., Valenti, J. A., Burrows, A., & Hora, J. L. 2008, *ApJ*, 684, 1427
Mandel, K., & Agol, E. 2002, *ApJ*, 580, L171
Markwardt, C. B. 2009, arXiv:0902.2850
McCullough, P. R., et al. 2006, *ApJ*, 648, 1228
Morales-Calderón, M., et al. 2006, *ApJ*, 653, 1454
Seager, S., Deming, D., & Valenti, J. A. 2008, arXiv:0808.1913
Spiegel, D. S., Silverio, K., & Burrows, A. 2009, arXiv:0902.3995
Zahnle, K., Marley, M. S., Lodders, K., & Fortney, J. J. 2009, arXiv:0903.1663

This preprint was prepared with the AAS L^AT_EX macros v5.2.

Table 1. Secondary eclipse best fit parameters

λ (microns)	Eclipse Depth ΔF	Eclipse Center Time (HJD)	Time offset ΔT (min)
3.6	0.00081 ± 0.00017	$2454421.10118 \pm 0.01675$	-6.9 ± 24.1
4.5	0.00098 ± 0.00020	$2454423.72707 \pm 0.01306$	7.8 ± 18.8
5.8	0.00167 ± 0.00036	$2454421.10719 \pm 0.01315$	1.8 ± 18.9
8.0	0.00133 ± 0.00049	$2454423.71817 \pm 0.01221$	-5.1 ± 17.6

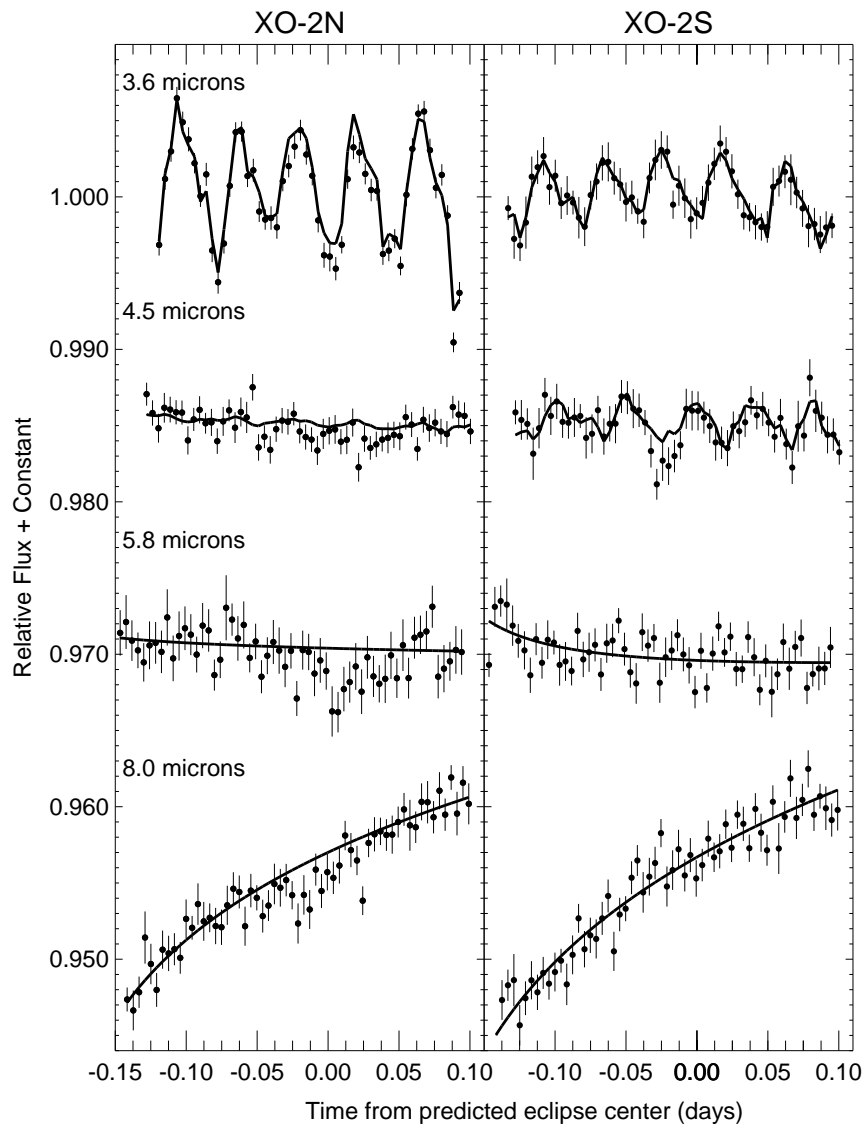


Fig. 4.— (left) Secondary eclipse observations of XO-2b with IRAC on *Spitzer Space Telescope* in 3.6 micron, 4.5 micron, 5.8 micron and 8.0 micron channels (from top to bottom) binned in 6.0-minute intervals and normalized to 1 and offset for clarity. XO-2b orbits XO-2N the northern component of XO-2 binary. (right) The light curve of the southern component XO-2S of the binary system (with no planet) plotted to the same scale and included for comparison. The overplotted solid lines do *not* represent a fit to the time series, but rather show the corrections for the detector effects (see text).

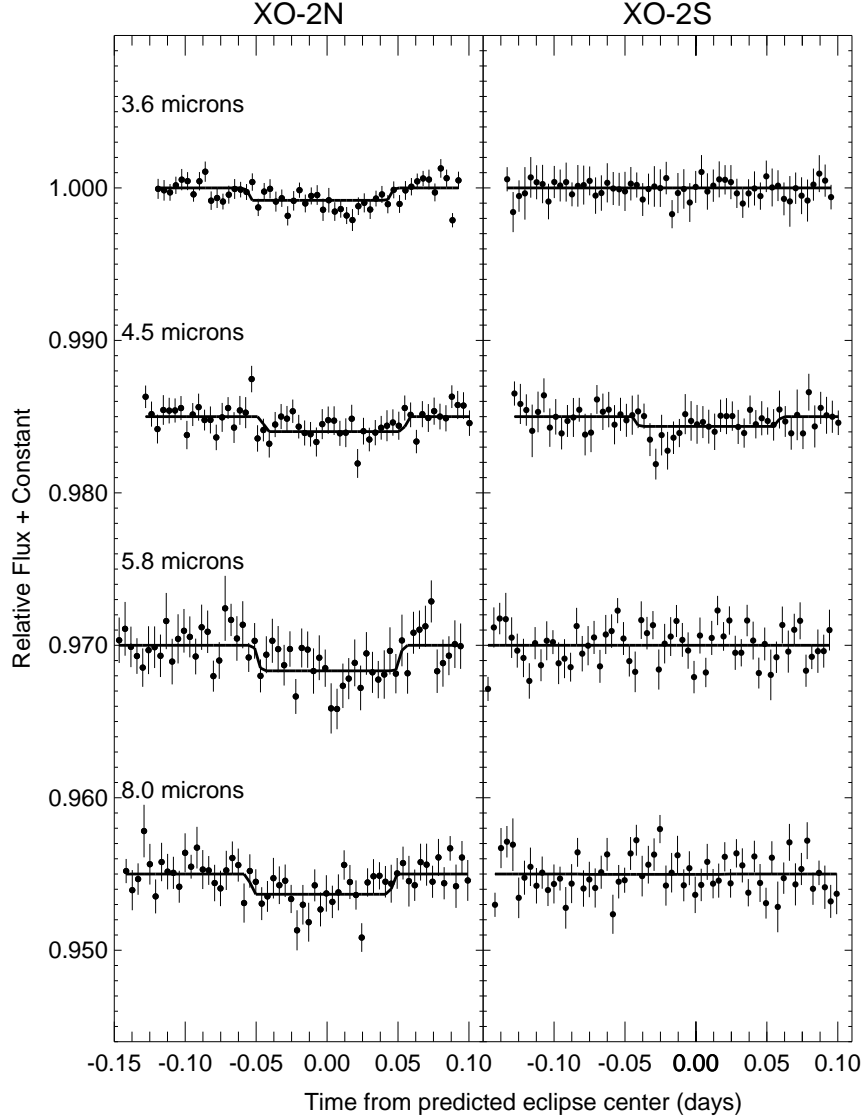


Fig. 5.— (left) Secondary eclipse of XO-2b around the binary component XO-2N observed with IRAC on *Spitzer Space Telescope* in 3.6, 4.5, 5.8, and 8.0 micron channels (top to bottom) corrected for detector effects, normalized and binned in 6.0-minute intervals and offset for clarity. The best-fit eclipse curves are overplotted. (right) The time series of the southern component XO-2S of the XO-2 binary, which has no eclipsing planet, after detector correction. The non-zero depth in the 4.5 micron channel of XO-2S is a spurious residual of systematic effects that mimics an eclipse. See §2.1 for details.

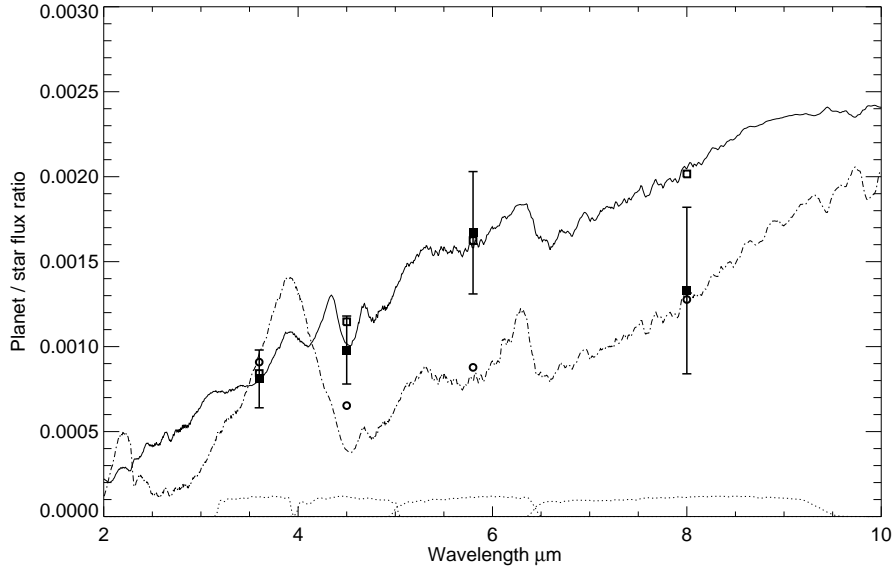


Fig. 6.— *Spitzer Space Telescope* IRAC secondary eclipse depths for XO-2b with MCMC error bars (filled squares). The predicted emission spectrum of the planet (Burrows et al. 2007a, 2008; Spiegel et al. 2009) with an upper atmospheric absorber of $\kappa_e = 0.1 \text{ cm}^2/\text{g}$ and redistribution parameter of $P_n=[0.3]$ is plotted as a solid line. A model with no atmospheric absorber and a redistribution parameters of $P_n=[0.3]$ is over plotted with dot-dashed line (see §3 for details). The band-averaged flux ratios are plotted as open squares and open circles for the models with and without an extra upper atmospheric absorber, respectively. The normalized *Spitzer Space Telescope* IRAC response curves for the 3.6-, 4.5-, 5.8-, and 8.0 micron channels are plotted at the bottom of the figure (dotted lines).